Research Article

Tahani Saad Algarni, Naaser A. Y. Abduh, Ahmed Aouissi*, and Abdullah Al Kahtani

Photodegradation of methyl orange under solar irradiation on Fe-doped ZnO nanoparticles synthesized using wild olive leaf extract

https://doi.org/10.1515/gps-2022-0077
received March 22, 2022; accepted August 22, 2022

Abstract: Fe-doped ZnO nanoparticles (NPs) with different Fe contents (0.1–5.0 wt%) were prepared using extract of wild olive leaves growing in Saudi Arabia (region of Abha). The biosynthesized NPs were characterized by Fourier transform infrared spectroscopy, X-ray diffraction, Brunauer–Emmett–Teller, scanning electron microscopy, transmission electron microscopy, and photoluminescence (PL). Characterization results showed that undoped ZnO and Fe-doped ZnO powders were crystallized in the wurtzite structure with a small shift for the doped samples. Neither Fe_3O_4 nor another iron oxide phase was observed in the samples, which proves the incorporation of Fe into the ZnO lattice. Doping has a pronounced effect on the physical and optical properties. Indeed, the size of the crystallites, the energy of the bandgap as well as the intensity of the PL emission decreased with the Fe content. Photocatalytic tests revealed that the doped samples degraded methyl orange (MO) more efficiently than pure ZnO and pure Fe_3O_4. Moreover, the photocatalytic activity improved with increasing Fe content. The best photocatalyst of the series (Fe–ZnO-5) was found degrading MO by 92.1%, in 90 min in a pseudo-first order reaction.

Keywords: Fe-doped ZnO nanoparticles, wild olive leaves, methyl orange, photodegradation, green synthesis

1 Introduction

Several industries including textiles, paper, plastics, and leather tanneries use synthetic dyes in large quantities [1,2]. Among these dyes, the azo compounds are the most abundant compounds (60–70%) in textile waste, which contributes significantly to water pollution [3]. Because of their toxicity, they generally pose a great threat to living aquatic organisms [4,5]. That is why research for their disposal of wastewater has been intensified. Methyl orange (MO), one of the azo dyes often used is non-biodegradable and therefore it can cause several pollution problems by generating toxic carcinogenic compounds in water [6]. Its degradation is therefore necessary because of its properties harmful to humanity [7]. Various methods physical [8,9], chemical [10,11], and biological [12] for removing azo dyes in wastewater have been explored. Unfortunately, in most cases these methods do not completely destroy the dye molecules [13–15]. Thus, it is necessary to develop an efficient method for their complete degradation. Advanced oxidation processes, whose principle is based on the production of hydroxyl radicals (·OH), are effective methods for the complete degradation of dyes. These methods using materials capable of collecting solar energy (photocatalysis) and mechanical energy (piezocatalysis) have found applications for wastewater treatment due to their efficiency and environmental friendliness [16–18]. It has proven to be the most efficient and environmentally friendly method for wastewater treatment. Thanks to this alternative, the pollutants are effectively mineralized into H_2O and CO_2. The degradation is carried out in the presence of a photocatalyst, according to an oxidation-reduction process without causing secondary pollution [19]. In the case of piezocatalysis, the mechanical vibrations, by increasing the number of free electrons and holes on the surface of the piezocatalyst, produce free radicals which decompose organic pollutants by oxidation [20].

On the other hand, in the case of photocatalysis the organic pollutants are decomposed by oxidation using

* **Corresponding author: Ahmed Aouissi,** Department of Chemistry, King Saud University, P.O. Box 2455, Riyadh-11451, Saudi Arabia; Chemistry Department, College of Science, King Saud University, Riyadh, Saudi Arabia, e-mail: aouissed@yahoo.fr
Tahani Saad Algarni, Naaser A. Y. Abduh, Abdullah Al Kahtani: Department of Chemistry, King Saud University, P.O. Box 2455, Riyadh-11451, Saudi Arabia; Chemistry Department, College of Science, King Saud University, Riyadh, Saudi Arabia

solar energy. The oxidation is triggered by photons whose energy matches or exceeds that of the bandgap of a given semiconductor [21]. In this process, where an electron is excited from the valence band (VB) to the conduction band (CB), a positive hole in the VB is formed due to the action of the $OH^{\cdot}$ radical with the OH^{-} ion in the water, which can then be used for oxidation. Meanwhile, the excited electron can reduce the oxygen in the CB, thereby acting as an oxidant [21]. Due to their instability in the excited state, the electrons generated can recombine in their respective holes. This causes dissipation of the input light energy and results in low efficiency of the photocatalyst. Photocatalysis is a cost-effective treatment method to get rid of toxic pollutants present in industrial wastes and has the advantage of degrading various chemical compounds under the action of sunlight.

In order to develop an effective photocatalyst, several metallic semiconductor materials have been explored as a photocatalyst [22]. Among these semiconductor materials, ZnO nanoparticles (NPs) have often been used because of their interesting properties compared to other nanomaterials. In addition, they are much more available and less expensive for wastewater treatment [23]. ZnO is a semiconductor that has a wide bandgap (about 3.37 eV) and a high excitation binding energy (60 mV). This allows the creation of electron–hole pairs under light irradiation. Unfortunately, its wide band limits its use in the UV region of sunlight [24,25]. An efficient photocatalyst must absorb visible radiation in addition to ultraviolet radiation because solar radiation is composed of a large proportion of visible radiation and a small proportion of ultraviolet radiation [26]. It is therefore essential to extend the optical absorption of ZnO from the UV region to the visible region for photocatalytic applications. Various approaches, including controlling the morphology and the size, coupling with other semiconductors, and doping with several elements have been explored to overcome this constraint. In the case of doping, several dopants were used including non-metals and transition metals [27]. Each dopant can induce a specific characteristic that can influence the properties of the photocatalyst. It is therefore possible by inserting transition metal ion dopants to enhance the photocatalytic properties of ZnO. Various photocatalytic semiconductors have been studied but their application in photocatalysis still remains on a laboratory scale. The difficulty of their industrial application is generally attributed to the low photocatalytic activity under solar lighting [28]. On the other hand, considerable research work has been done to improve the photocatalytic properties. Iron-based oxides have the advantage of having a narrow bandgap, making it easier to absorb photons in the visible region, thus increasing the visible light absorption of ZnO by narrowing the bandgap. By doping zinc oxide having a large surface area with iron oxide having a smaller bandgap, an efficient solar photocatalyst can be developed. This work aims to develop an environmentally friendly photocatalyst for wastewater treatment, operating under conditions similar to those encountered in the natural environment. In order to reach this goal, ZnO and Fe/ZnO nanomaterials were synthesized by a green procedure using wild olive leaf extract and were fully characterized via X-ray diffraction (XRD), transmission electron microscopy (TEM), scanning electron microscope (SEM), Brunauer–Emmett–Teller (BET) surface analysis, and UV-visible (UV-Vis) spectrophotometer. To our knowledge, the synthesis of Fe-doped ZnO nanomaterials by a procedure using an extract of wild olive leaves growing in Saudi Arabia (Abha region) is a work that has not been studied before. The efficiency of the photocatalysts was evaluated in the degradation of MO under direct sunlight irradiation.

2 Materials and methods

2.1 Materials

Wild olive leaves were collected from Abha region in southern Kingdom of Saudi Arabia. Zn $(NO_3)_2{\cdot}6H_2O$ powder (>99%), NaOH (98%), and $C_{14}H_{14}N_3NaO_3S$ (MO, 99.8%) were purchased from British Drug Houses Chemicals Ltd, Poole, England. All of these chemicals were used as received.

2.2 Preparation of leaf extract

Undamaged wild olive leaves were washed in deionized water and dried in the shade for 2–3 weeks. After cutting them into small pieces, 10 g of these pieces are dissolved in 100 mL of deionized water, boiled at 60°C for 15 min to kill the pathogens in the solution. Then, this aqueous leaf extract solution was cooled, filtered through filter paper, and stored at 4°C for later use.

2.3 Synthesis of ZnO NPs

The preparation of the ZnO NPs was carried out as follows: 5 g zinc nitrate were added to the 30 mL of extract and stirred for 2 h. 16 mL of NaOH (3.5 M) were added dropwise, the resulting solution was heated to 75°C

with stirring in a closed container for 5 h. The precipitate thus formed was separated from the solution by filtration and washed several times with an aqueous solution of ethanol with a water/ethanol ratio of 1/3. The nanomaterial thus obtained was dried in an oven at 60°C overnight and then calcined in a furnace at 500°C for 3 h.

2.4 Synthesis of Fe-dopped ZnO NPs

In order to prepare Fe-dopped ZnO NPs, desired amount of zinc nitrate and iron(III) chloride was added into 30 mL of the extract and stirred for 2 h. 18 mL of NaOH (3.5 M) were added dropwise, the resulting mixture was heated to 75°C with stirring in a closed vessel for 5 h. The precipitate formed is separated and washed several times with an aqueous solution of ethanol in a water/ethanol proportion of 1/3. Then, it was put in the oven at 60°C overnight. The resulting nanomaterial was then calcined at 500°C for 3 h. A series of Fe-doped ZnO with different Fe contents (Fe: 1%, 2%, 3%, 4%, 5%, and 7%) were prepared. They are denoted as Fe–ZnO-x where x is the mass percentage of Fe in the Fe–ZnO photocatalyst: Fe–ZnO-1, Fe–ZnO-2, Fe–ZnO-3, Fe–ZnO-4, Fe–ZnO-5, and Fe–ZnO-7.

2.5 Photocatalytic experiment

The photo degradation of MO was carried out under solar irradiation at atmospheric pressure. Typically, 50 mg NPs catalyst were added into a beaker containing MO dye solution (10 mL, 10 mg·L^{-1}). Prior to exposure to sunlight, the suspension was magnetically stirred in the dark for 30 min to reach the adsorption–desorption equilibrium. The experiment was carried out on a sunny day (outside temperature 40°C, sunlight intensity in the range of 15–25 mW·cm^{-2}). A control solution was prepared and kept under similar conditions to see if there was any color change in the MO dye solution. At given time intervals, 10 mL of suspension was sampled and centrifuged (7,000 rpm) for 10 min, the supernatant was collected for absorption analysis on a UV-Vis spectrophotometer. The photocatalytic degradation of MO was followed by the gradual decrease in absorption intensity at λ_{max} = 464 nm and a wavelength scan ranging from 600 to 350 nm.

The photodegradation of MO was conducted under solar irradiation at atmospheric pressure. Typically, to a beaker containing 10 mL of MO aqueous solution, 50 mg NPs catalyst are added gradually. Before exposure to sunlight, the suspension is stirred magnetically in the dark for 30 min to reach adsorption–desorption equilibrium. The experiments were carried out on sunny days at a temperature of about 40°C and a sunlight intensity in the range of 15–25 mW·cm^{-2}. A control solution was prepared and exposed under similar conditions to see if there was a color change in the MO solution. At given periods of time, 10 mL of suspension are taken and centrifuged (7,000 rpm) for 10–15 min. The supernatant is then separated and analyzed using a UV-Vis spectrophotometer. The photocatalytic degradation of MO was followed by the gradual decrease in absorption intensity at λ_{max} = 464 nm and a wavelength sweep ranging from 600 to 350 nm.

The MO photodegradation rate was determined using Eq. 1:

$$\text{Degradation } \% = \frac{A_o - A_t}{A_0} \quad (1)$$

where A_0 represents the initial absorbance of MO and A_t the absorbance of the solution at time t after solar irradiation.

2.6 Characterization of the photocatalysts

The optical and structural properties of the prepared undoped ZnO and Fe-doped ZnO NPs were characterized by various technics. Functional groups of the compounds were examined by using Fourier transform infrared spectroscopy (FTIR). Infrared spectra were recorded with an infrared spectrometer Genesis II FTIR (4,000–350 cm^{-1}) using the KBr Pellet technique. The crystal structure of the nanomaterials was examined by an XRD, using an Ultima IV X-ray Rigaku diffractometer using Cu-Kα radiation. The data were collected over a 2θ range of 20–80°. TEM micrographs were performed on a JEOL JEM-2100F field emission electron microscope (JEOL, Japan) with an acceleration voltage of 110 kV. Surface morphology of the catalysts were determined by means of a Scanning Electron Microscopy (SEM) on a JEOL JSM-7600F) (JEOL, Japan) with an accelerating voltage of 100 V and a beam current of 30A. UV-Vis analysis was performed by using a double beam UV-Vis. The specific surface area (BET) was measured by a Micromeritics Tristar II 3020 surface area and porosity analyzer. The fluorescence spectra were measured using Shimadzu RF-6000 fluorescence spectrophotometer. Particle aqueous suspension was sonicated for 30 min. The excitation wavelength was 320 nm and the fluorescence spectra were recorded in the wavelength

range from 300 to 600 nm. A pass width of 10 nm was used for the measurement of the emission and excitation spectra.

3 Results and discussion

3.1 Catalysts characterization

3.1.1 FTIR

An FTIR study was performed to determine the major functional groups present in wild olive leaf extract (WOLE) to suggest biomolecules responsible for reducing and capping Zn^{2+} leading to the formation of ZnO NPs. The WOLE spectrum shows the presence of a multitude of absorption peaks, indicating its complex nature. The spectrum is shown in Figure 1. The IR bands at 3,405 and 1,710 cm^{-1} in WOLE are due to the O–H and C═O stretching modes of the OH group and the C═O group, respectively [25,26]. The strong band observed at 2,931 cm^{-1} seems to be due to the –CH stretching vibrations of the methyl and methylene groups. The peak at 1,635 cm^{-1} is characteristic of the CO, C–O, and O–H groups. The band at 1,635 cm^{-1}, due to the C–O stretch, indicates the probable presence of carboxyl coupled to the amide bond in amide I and the band at 1,517 cm^{-1}, due to NH stretching, indicates the presence of amide II. The band at 1,405 cm^{-1} is attributed to methylene vibrations. The intense band at 1,075 cm^{-1} can be attributed to C–N stretching vibrations of aliphatic amines [29] or C–OH vibrations in the WOLE [30]. Bands at 930 and 765 cm^{-1} may be due to C–N stretching amine groups [31]. The 3 small peaks at 618, 542, and 765 cm^{-1} can be assigned to the C–H bend [32]. The results of the present study suggest that the amine (N–H), hydroxyl (–OH), and carboxyl (–C═O) groups evidenced by the FTIR could be responsible for the reduction and stabilization of the ZnO NPs.

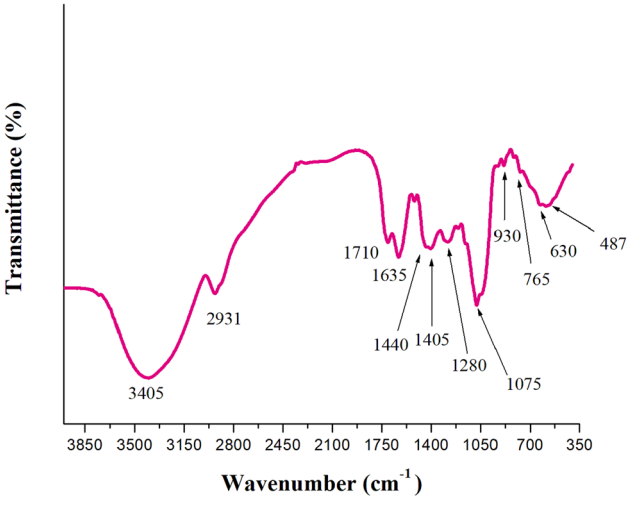

Figure 1: FTIR spectrum of WOLE.

Figure 2 depicts the FTIR spectrum of ZnO and Fe-doped ZnO NPs. FTIR bands of ZnO NPs appear between 441 and 665 cm^{-1} [33]. The strong peaks at 442 cm^{-1} can be ascribed to the vibrational modes of the Zn–O bonds as reported in the literature [34]. The strong peak at 442 and 565 cm^{-1} can be attributed to the vibration of Zn–O bond and confirms the formation of product [35]. It has been reported in the literature that these bands can be ascribed to the stretching vibration of Zn–O bond [34,36]. The band at 665 cm^{-1} is assigned to the Fe–O stretching. Based on similar FTIR results [37], the insertion of iron at the position of zinc in the ZnO fraction can be confirmed. It is important to note the shift of the peaks of the FTIR spectrum of the NPs compared to the leaf extract such as for example from 3,455 to 3,405, from 1,635 to 1,630, from 1,075 to 1,040, and from 930 to 910 cm^{-1}. This indicates the possible involvement of alcohols, amines, carboxylic acids, ketones, and polyols in the bioreduction of metal ions [38]. In fact, it has been reported that similar functional groups of heterocyclic compounds present in the leaf extract are used as capping ligands [39].

3.1.2 XRD analysis

The XRD patterns for ZnO, Fe_3O_4, and Fe-doped ZnO samples calcined at 500°C are shown in Figure 3. The result

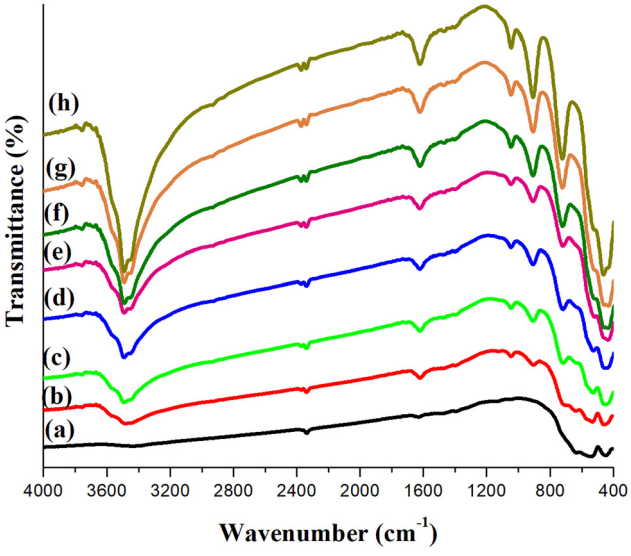

Figure 2: FTIR spectra of: (a) Fe_3O_4, (b) ZnO, (c) Fe–ZnO-1, (d) Fe–ZnO-2, (e) Fe–ZnO-3, (f) Fe–ZnO-4, (g) Fe–ZnO-5, and (h) Fe–ZnO-7.

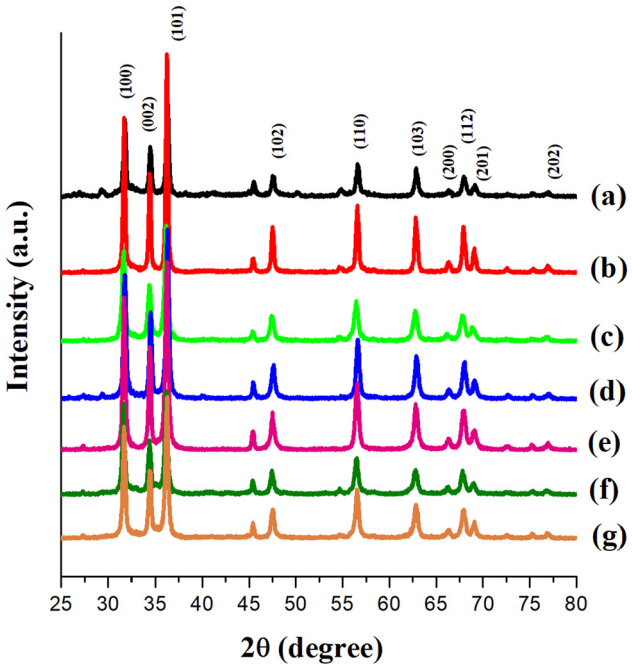

Figure 3: XRD pattern of: (a) ZnO, (b) Fe–ZnO-1, (c) Fe–ZnO-2, (d) Fe–ZnO-3, (e) Fe–ZnO-4, Fe–ZnO-5, and (g) Fe–ZnO-7.

shows the presence of crystallite peaks at 2θ = 31.79°, 34.45°, 36.29°, 47.58°, 56.63°, 62.89°, 66.37°, 67.98°, 69.10°, and 77.05° corresponding to the reflections of planes (100), (002), (101), (102), (110), (103), (200), (112), (201), and (202), designating the polycrystalline hexagonal wurtzite structure [JCPDS file no. 36–1451]. The peak which appears at 45.5° corresponds to $Zn(OH)_2$ [40,41]. It is due to the absorption of moisture induced by the high surface area. As for the Fe-doped Zinc oxide samples, a small shift in the position of the peaks was observed. For example, for Fe–ZnO-5, the peaks were observed at 2θ = 31.72°, 34.42°, 36.22°, 47.53°, 56.56°, 62.84°, 66.30°, 67.93°, 69.04°, and 76.94°. This result is in agreement with that of ref. [42]. Neither the Fe_3O_4 phase nor another iron oxide phase was observed. This proves that Fe has indeed been inserted into the lattice of ZnO. The decrease in crystallite size may be due to the smaller ionic radius of Fe^{3+} (0.064 nm) compared to Zn^{2+} (0.074 nm).

3.1.3 TEM

Figure 4 shows the TEM micrographs of the biosynthesized ZnO and ZnO doped with Fe. The images of the ZnO NPs (Figure 4a) confirm the nanometric scale of the biosynthesized nanomaterials and show that the NPs have a uniform distribution with a spherical shape and with very little aggregation. In addition, TEM images show that ZnO NPs have smooth surfaces and that the size of the NPs varied from 86 to 170 nm. TEM images of Fe-doped ZnO (Figure 4b) showed that the material obtained is heterogeneous and consists of a mixture of NPs of spherical and rod shape with a length varying between 123 and 170 nm. Fe-doped ZnO exhibits more aggregation than pure ZnO. This result indicates that the shape and the size depend strongly on the doping.

3.1.4 SEM with analysis

SEM micrographs of pure ZnO and iron-doped ZnO are depicted in Figure 5. From the micrograph (Figure 5a), it appears that the morphology of pure ZnO NPs tends toward the spherical shape. ZnO particles are well distributed with very low aggregation. As noted, ZnO particles do

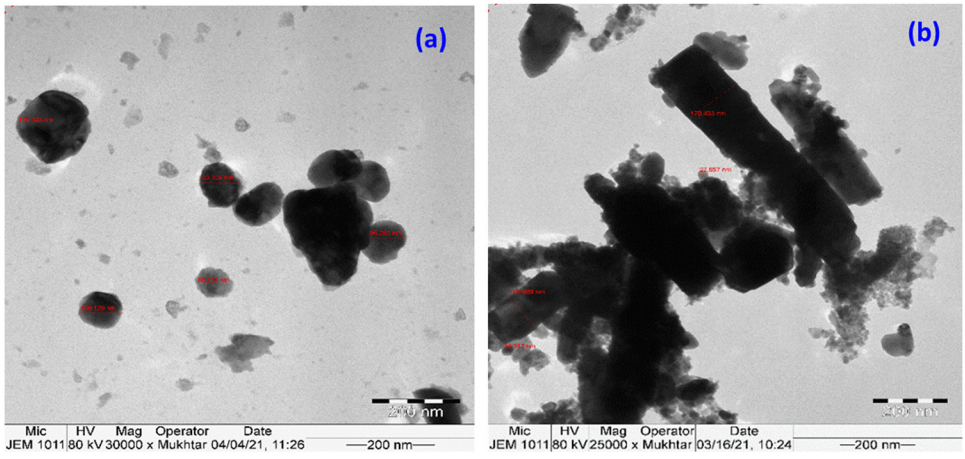

Figure 4: TEM micrographs of: (a) undoped ZnO and (b) ZnO-Fe-5.

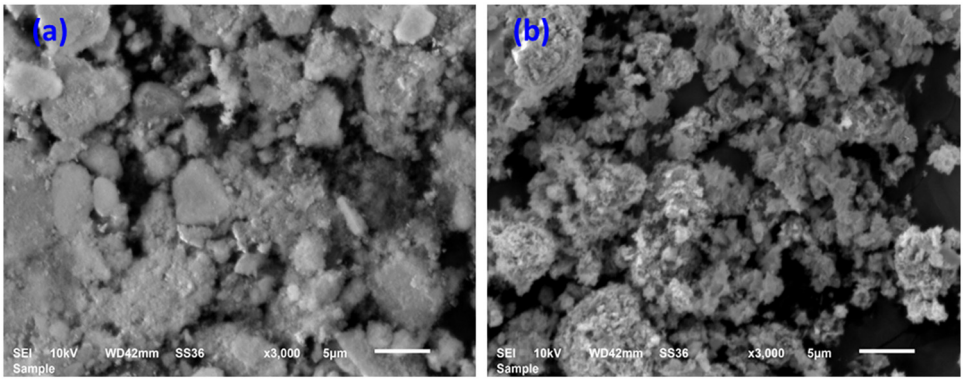

Figure 5: SEM images of: (a) undoped ZnO and (b) ZnO-Fe-5.

not have a uniform size distribution. As for Fe–ZnO-5 (Figure 5b), the image shows an overall porous and rough shape with some aggregations but with a large number of particles smaller than that of pure ZnO.

3.1.5 Bandgap determination

The optical bandgap (E_g) is one of the properties of semiconductor materials which can be greatly influenced by the doping and the size of the NPs. To estimate its value, the UV-Vis spectroscopy is the most used technique. This method was used to follow the evolution of the bandgap value after doping the pure ZnO by iron cation Fe^{3+}. The bandgap value of the undoped and doped ZnO samples were evaluated using the Tauc equation:

$$(\alpha h\nu)^{1/n} = A(h\nu - E_g) \quad (2)$$

where h, ν, and α account for Planck's constant, frequency, and absorption coefficient, respectively. A is the proportionality constant and n indicates the type of electronic transition (for permitted transitions, $n = 1/2$).

The results (Figure 6 and Table 1) show that the bandgap value of iron-doped ZnO is equal to 3.18 eV. This value is within the range of reported values for pure ZnO NPs [43]. The energy bandgap of the Fe-doped ZnO is slightly lower than that of undoped ZnO. As reported in the literature [44], the substitution of Zn^{2+} by Fe^{3+} increases the number of oxygen vacancies and energy levels, which decreases the energy gap.

3.1.6 Photoluminescence (PL) measurements

The influence of Fe doping on the physical properties of ZnO NPs was investigated by PL analysis. It is well known that the absorbance is related to different parameters such as the size of the NPs, the lack of oxygen, the bandgap, and the defects present in the structure [45]. Figure 7 shows the PL spectra of pure samples of ZnO, Fe–ZnO-3, and Fe–ZnO-5 obtained using ultraviolet light with a wavelength of 320 nm as an excitation source. These spectra show 2 peaks appearing at 363 and 409 nm. As it can be seen, the position of the peaks remains unchanged for each of the samples; the pure ZnO and the Fe-doped ZnO. The first peak observed at 363 nm is assigned to the near band edge [46,47] resulting in the band-to-band transition. The second peak (a shoulder) appearing around 409 nm is attributed to the recombination of an electron–hole pair in the Zn vacancy [48]. It is worth noting that the intensity of the peaks decreases after doping and it decreases further when the doping amount is increased. This can be explained by the fact that when Fe^{3+} is inserted in the ZnO lattice it induces defects, especially increases

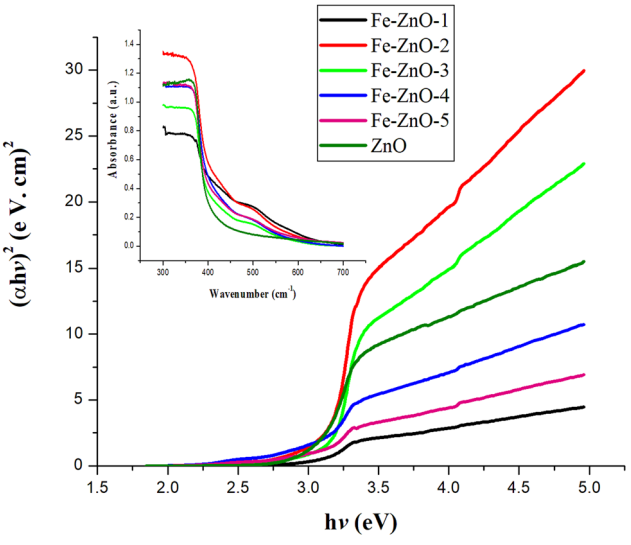

Figure 6: Optical band gab of undoped ZnO and Fe–doped ZnO nanoparticles with different Fe contents (0.1–5.0 wt%).

Table 1: Crystallite size and bandgap value of the undoped ZnO and Fe-doped ZnO metal oxide NPs

Photocatalyst	Physical properties	
	Crystallite size* (nm)	Bandgap (eV)
ZnO	22.50	3.18
ZnO-Fe-1	22.14	3.15
ZnO-Fe-2	21.46	3.14
ZnO-Fe-3	21.00	3.12
ZnO-Fe-4	20.25	3.09
ZnO-Fe-5	21.06	3.05
ZnO-Fe-7	15.49	3.14

*The values of crystallite size have been calculated by the Scherrer's equation.

oxygen vacancies which ultimately increases the energy levels localized near the VB.

3.2 Photocatalytic activity of ZnO and Fe_3O_4

To investigate the influence of Fe dopant content on the catalytic activity of undoped ZnO, first the photoactivity of both pure Fe_3O_4 and pure ZnO was evaluated. The degradation of MO by photolysis and by photocatalysis in the presence of pure ZnO and Fe_3O_4 were followed by the discoloration of the MO dye solution under sunlight for 45 min. The results obtained (Figure 8) show that in the absence of photocatalyst, the degradation of the MO dye is negligible. This indicated that the effect of photolysis on the MO dye is insignificant. In the dark,

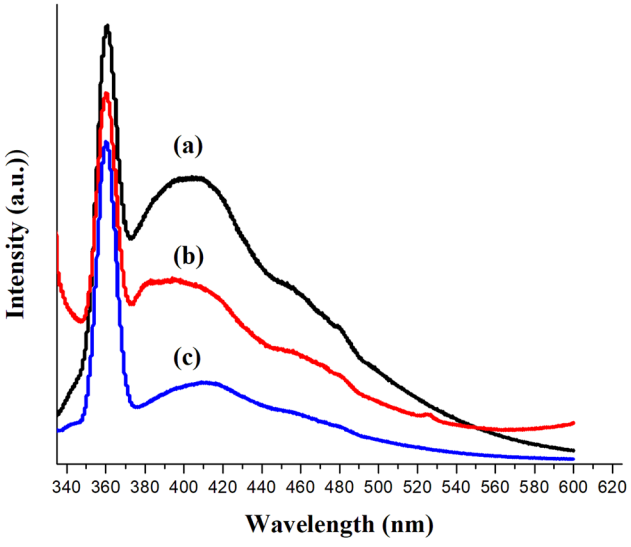

Figure 7: PL spectra of: (a) undoped ZnO, (b) Fe–ZnO-3, and (c) Fe–ZnO-5.

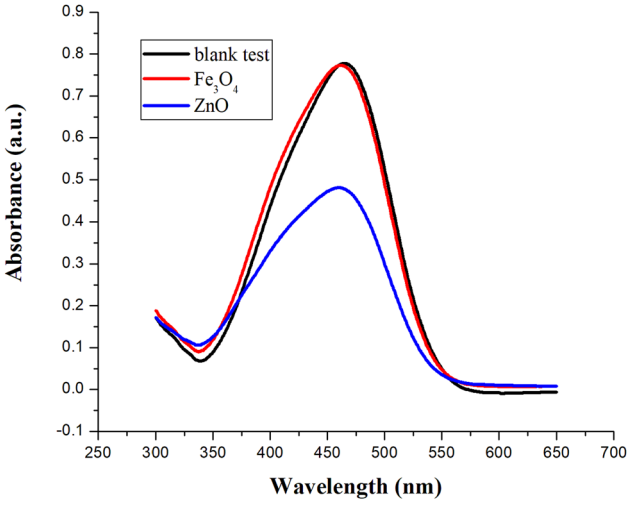

Figure 8: UV-visible absorbance spectra of degraded MO-dye under sunlight irradiation for 45 min over pure ZnO and Fe_3O_4.

only a slight decrease in MO absorbance was observed when the experiment was conducted in the presence of pure ZnO and Fe_3O_4 separately. This could be due to the adsorption on the surface of the NPs. Under the sunlight, the results showed that undoped ZnO is about 10 times more efficient than Fe_3O_4. In fact, ZnO degraded 40.7% of MO in 45 min, while Fe_3O_4 only degraded 4.7% in the same irradiation time. One of the causes of the low photoactivity of Fe_3O_4 compared to ZnO, is the rapid recombination of the electron–hole pairs of Fe_3O_4.

3.3 Photocatalytic activity of Fe-doped ZnO

The effect of Fe content on the photocatalytic degradation of aqueous MO solution under solar irradiation is depicted in Figure 9. As can be seen from the figure, all Fe-doped ZnO samples show an activity higher than that of pure ZnO and that of pure Fe_3O_4. Regarding the amount of Fe dopant on ZnO, it can clearly be seen that the photocatalytic activity increases with increasing amount of Fe up to a Fe content equal to 5%. Beyond this content, a decay was observed. So, the ZnO oxide doped with 5% iron is the most efficient photocatalyst of the series. The low photocatalytic activity of ZnO under the action of sunlight is due to its wide bandgap, only allowing the use of sunlight at the region of UV light. As for the low activity of Fe_3O_4, it is due to the rapid recombination of photogenerated electrons and holes. When Fe ions are used as dopants (in small amounts), they were inserted into the ZnO matrix and can therefore serve as trap centers for the capture of electrons or holes [49,50]. This result is

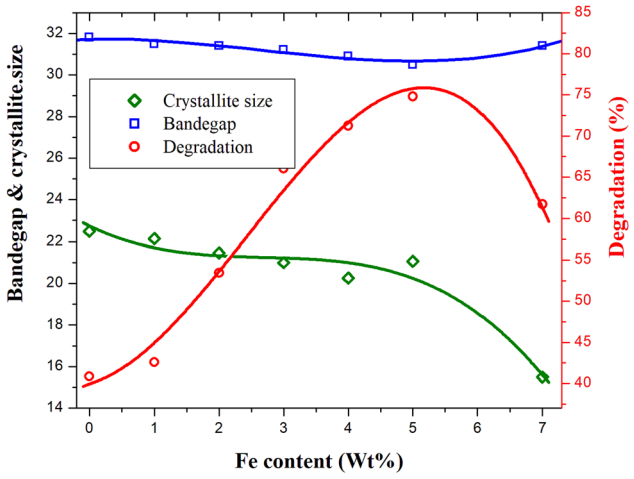

Figure 9: Effect of Fe content on bandgap, crystallite size, and MO degradation. The photodegradation was carried out under solar irradiation for 45 min.

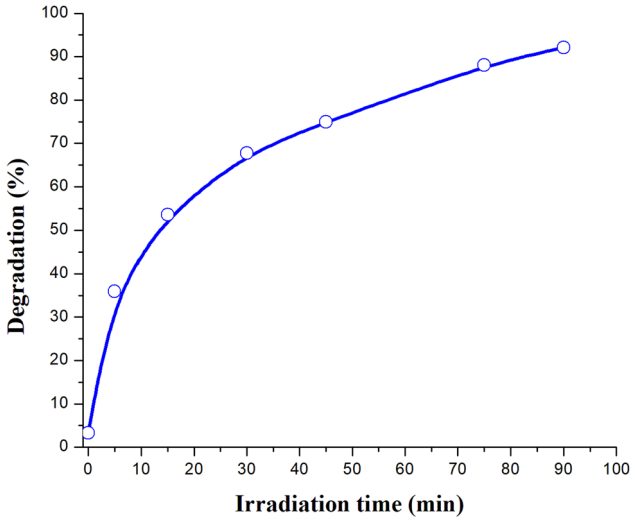

Figure 10: Degradation as a function of irradiation time of MO dye under solar irradiation on Fe–ZnO-5.

corroborated by UV and XRD characterizations (Table 1) where it was observed that iron-doped ZnO solids exhibit a lower bandgap and crystallite size than pure ZnO. Similar results have been reported in the literature. Huang et al. [51] reported that doping with Fe^{3+} ions improve the separation of electron–hole pairs due to the decrease in the bandgap, resulting in a shift of the absorption towards the visible light spectrum and it also decreases the particle size. In their study on arrays of Fe-doped ZnO nanorods with different doping amounts, Xiao et al. [52] observed better photocatalytic activity for 1.0% Fe-doped ZnO nanorods. Ba-Abbad et al. [53] also explained the enhancement of photocatalytic activity by the reduction in the particle size by adding small amounts of Fe dopant. It should be emphasized that other factors can also make a contribution, but little, to the performance of photocatalytic activities. Indeed, it has been reported that the photocatalytic activity is related to the bandgaps, to the nanosized structures, and to the surface areas [54,55]. Based on the above discussion, the photocatalytic activity enhancement of Fe-doped samples may also be due to the high specific surface area in addition to the decrease in the bandgap. In fact, Fe-doped ZnO (ZnO-Fe-5) has a BET surface area of 16.23 $m \cdot g^{-2}$, while pure ZnO has only a surface area of 3.68 $m \cdot g^{-2}$. It could then be said that Fe doping improves the activity by decreasing the bandgap energy and crystallite size and also increasing the surface area.

3.3.1 Effect of irradiation time

Figure 10 represents the effect of irradiation time on MO degradation over the best photocatalyst of the series, namely, Fe–ZnO-5. The result shows that the degradation rate of MO dye increased when the irradiation time increased from 0 to 90 min, indicating that the reduction/decomposition process of MO dye is carried out by Fe–ZnO-5 NPs. After 90 min of solar radiation, the degradation of the MO dye reaches 92.1%. This clearly shows the efficiency of Fe–ZnO-5 photocatalyst for MO dye photodegradation.

3.3.2 Kinetic study

The degradation of MO catalyzed by Fe–ZnO-5 proceeds in two steps. In the first one, the MO molecule is adsorbed on Fe–ZnO-5 and in the second step, the degradation reaction is triggered. Information on the adsorption mechanism of a heterogeneous surface reaction can be obtained from the kinetics of the adsorption process described by the Langmuir–Hinshelwood mechanism for surface catalyzed reactions [56,57]. This process can be detailed by two basic mechanisms:

(i) successive attacks of the coloring matter by the hydroxyl radical ($HO^{\cdot}$) leading to its oxidation.
(ii) reaction of the dye with generated holes.

When MO molecules and one of the oxygen-containing species are adsorbed on neighboring sites, an oxygen in its molecular form on the surface of the Fe-doped ZnO can play the role of an electron acceptor, thus leading via the superoxide radical O_2^- to the hydrodioxyl radical ($HO_2^{\cdot}$) formation known as a precursor of $HO^{\cdot}$ radical [58].

In the case where the degradation of the MO dye in aqueous solution over Fe–ZnO oxide catalyst obeys the kinetics of a pseudo-first order reaction, the description according to Langmuir–Hinshelwood mechanism is as follows:

$$r = \frac{dc}{dt} = k_1 \frac{KC}{1 + KC} \quad (3)$$

$$r = \frac{K_{app} C}{1 + KC} \quad (4)$$

where k accounts for the intrinsic rate constant, K is the Langmuir–Hinshelwood adsorption equilibrium constant, K_{app} ($k.K$) is the apparent rate constant, and C is the concentration of MO at time t.

After approximation ($KC \ll 1$) and integration, the above rate expression gives the pseudo-first-order equation:

$$\ln \frac{C_o}{C_t} = k_{app} t \quad (5)$$

The curve $\ln(C_o/C_t)$ representing the photodegradation with time of MO by Fe–ZnO-5 photocatalyst under sunlight irradiation is represented in Figure 11. The curve obtained is a straight line with a correlation constant $R^2 = 0.9832$. As the correlation constant for a straight line must be $R^2 > 0.95$, the kinetics of the MO degradation reaction in the presence of Fe–ZnO-5 is of pseudo first-order. The value of the rate constant determined from the slope of the curve is 0.0254 min^{-1}. This value further indicates that the Fe–ZnO-5 photocatalyst has good photocatalytic reactivity which corroborates the MO degradation efficiency.

3.3.3 Effect of catalyst loading

To investigate the effect of the amount of catalyst on MO photodegradation, experiments were performed by varying the Fe–ZnO-5 photocatalyst loading from 0.25 to 2.00 $g{\cdot}L^{-1}$. The dye concentration was kept to 0.03 mM and the duration of irradiation was for 40 min. The results showed that the percentage of MO degradation increased from 58.9% to 95.3% when the catalyst loading increased from 0.25–2.00 $g{\cdot}L^{-1}$ (Figure 12). The increase in the degradation rate with the loading of Fe–ZnO-5 is due to the increase in the number of active sites. In fact, the increase in the latter leads to an increase in the hydroxyl radicals formed, thus leading to an increase in the number of degraded dye molecules. It should be mentioned that the use of a large amount of catalyst increases the turbidity of the solution which limits the penetration of UV light into the reaction mixture and thus leads to a decrease in the reaction rate. This is why the experiments were carried out with small quantities in order to avoid the turbidity of the solution.

3.3.4 Reusability

Recycling of photocatalysts is one of the important processes as it contributes to economic and environmental development. Thus, the photocatalytic stability of a photocatalyst for its reuse is a critical factor, especially for large-scale applications. In order to study the stability of the biosynthesized Fe–ZnO-5 photocatalyst, experiments for

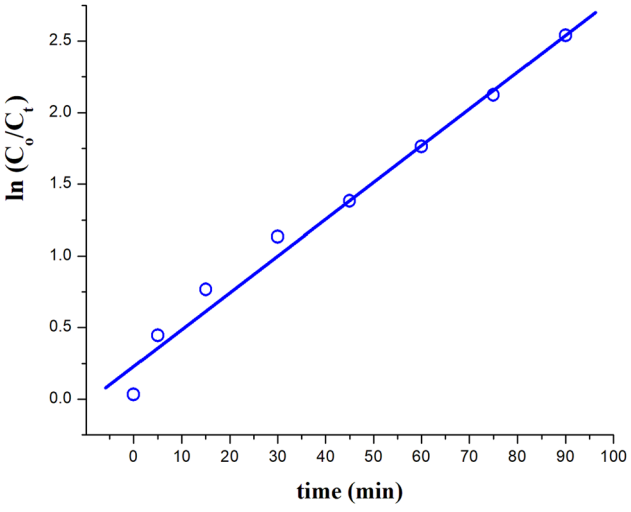

Figure 11: Kinetics of MO-dye photodegradation over Fe-ZnO-5 under sunlight irradiation.

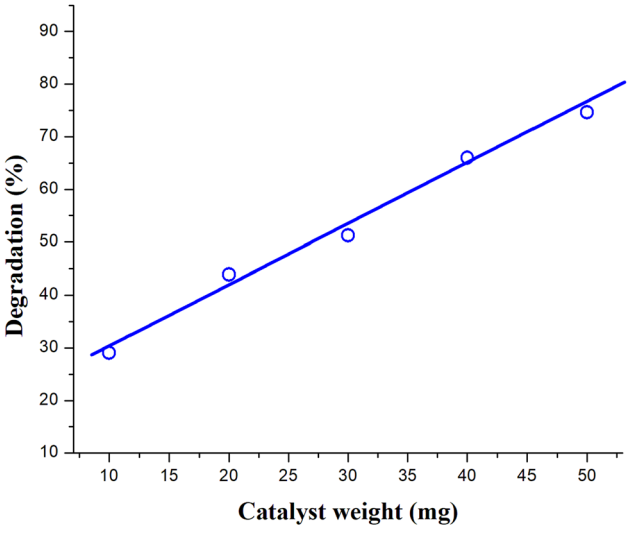

Figure 12: Effect of Fe–ZnO-5 photocatalyst loading on MO dye degradation under solar irradiation.

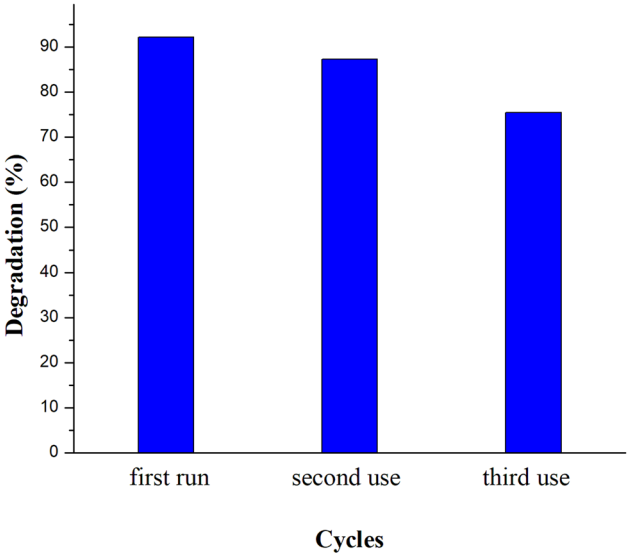

Figure 13: Recycling efficiency of Fe–ZnO-5 photocatalyst on MO dye degradation under solar irradiation.

its recycling for MO dye degradation were conducted under the same conditions. After each experiment, Fe–ZnO-5 is recovered from the aqueous MO solution by centrifugation, washed three times with an ethanol–acetone solution (1:1 by volume), and then placed in an oven at 80°C overnight to be reused. The recovered Fe–ZnO was reused twice, and the results (Figure 13) obtained show that the fresh Fe–ZnO-5 sample degraded the MO by 92.1%, while in the case of its second and third use, it has degraded the MO by 87.3% and 75.4%, respectively. This slight decrease in the rate of degradation was expected, indeed, many studies have shown that the photocatalytic activity decreases after repeated use [59,60]. These results therefore confirm that Fe–ZnO maintained an acceptable performance allowing it to be used successfully for the removal of MO dye in wastewater.

4 Conclusion

ZnO and iron-doped ZnO NPs were biosynthesized by a simple method using WOLEs. They have been characterized and tested for MO degradation using sunlight. The effects of Fe doping content on physical and photocatalytic properties were investigated.

The shift evidenced by the FTIR analysis for the obtained peaks suggests that the amine (NH), hydroxyl (–OH), and carboxyl (–C═O) groups could be involved in the reduction and stabilization of the ZnO NPs.

Fe doping leads to a reduction in the size of ZnO crystallites without modifying the crystal structure of ZnO. The absence of Fe_3O_4 or any Fe(III)-oxide phase in the XRD pattern indicates that Fe^{3+} has been inserted into the ZnO.

The TEM image reveals that the ZnO NPs have a spherical shape and do not show aggregation, while the Fe-doped ZnO NPs consist of a mixture of spherical and rod shape showing aggregation. This result clearly indicates that the size and shape of the NPs strongly depend on the doping.

Fe doping decreased the bandgap energy of ZnO and as the Fe content increased, the bandgap decreased. This may suggest that the substitution of Zn^{2+} by Fe^{3+} causes the formation of oxygen vacancies resulting in additional energy levels, thus reducing the bandgap.

The enhanced photocatalytic performance of doped ZnO NPs is the result of Fe doping which reduced the bandgap energy and crystal size and increased surface area.

Funding information: The authors extended their appreciation to the Deanship of Scientific Research at King Saud University: Grant Number RG-1441-507.

Author contributions: Naaser A.Y. Abduh carried out the photocatalytic tests and the chromatographic analyses. Tahani Al-Garni collected the olive leaves and carried out the characterizations of the prepared photocatalysts. Abdullah Al Kahtani as head of laboratory provided the equipment and the necessary funding for the realization of this work, Ahmed Aouissi planned the realization of this work and wrote the article. All authors have read and accepted the published version of the manuscript.

Conflict of interest: Authors state no conflict of interest.

References

[1] Ito T, Adachi Y, Yamanashi Y, Shimada Y. Long–term natural remediation process in textile dye-polluted river sediment driven by bacterial community changes. Water Res. 2016;100:458–65.

[2] Liu J, Peng G, Jing X, Yi Z. Treatment of methyl orange by the catalytic wet peroxide oxidation process in batch and continuous fixed bed reactors using Fe-impregnated 13X as catalyst. Water Sci Technol. 2018;78:936–46.

[3] Aziztyana AP, Wardhani S, Prananto YP, Purwonugroho D. IOP conference series. Mater Sci Eng. IOP Publishing; 2019. p. 042047.

[4] Ozdemir O, Armagan B, Turan M, Celik MS. Comparison of the adsorption characteristics of azo-reactive dyes on mezoporous minerals. Dye Pigment. 2004;62:49–60.

[5] Wang S, Li H, Xie S, Liu S, Xu L. Physical and chemical regeneration of zeolitic adsorbents for dye removal in wastewater treatment. Chemosphere. 2006;65:82–7.
[6] Khatri J, Nidheesh PV, Singh TA, Kumar MS. Advanced oxidation processes based on zero-valent aluminium for treating textile wastewater. Chem Eng J. 2018;348:67–73.
[7] Zou H, Wang Y. Functional collaboration of biofilm-cathode electrode and microbial fuel cell for biodegradation of methyl orange and simultaneous bioelectricity generation. Env Sci Pollut R. 2019;26:23061–9.
[8] Garrido-Cardenas JA, Esteban-García B, Agüera A, Sánchez-Pérez JA, Manzano-Agugliaro F. Wastewater treatment by advanced oxidation process and their worldwide research trends. Int J Env Res Pub He. 2020;17:170.
[9] Al-Baldawi IA, Abdullah SRS, Almansoory AF, Ismail NI, Hasan HA, Anuar N. Role of Salvinia molesta in biodecolorization of methyl orange dye from water. Sci Rep-Uk. 2020;10:1–9.
[10] Sen SK, Raut S, Bandyopadhyay P, Raut S. Fungal decolouration and degradation of azo dyes: a review. Fungal Biol Rev. 2016;30:112–33.
[11] Wang S, Yun J-H, Luo B, Butburee T, Peerakiatkhajohn P, Thaweesak S, et al. Recent progress on visible light responsive heterojunctions for photocatalytic applications. J Mater Sci Technol. 2017;33:1–22.
[12] Guo Q, Zhou C, Ma Z, Yang X. Fundamentals of TiO2 photocatalysis: concepts, mechanisms, and challenges. Adv Mater. 2019;31:1901997.
[13] Muhd Julkapli N, Bagheri S, Bee Abd Hamid S. Recent advances in heterogeneous photocatalytic decolorization of synthetic dyes. Sci World J. 2014;2014.
[14] Minas F, Chandravanshi BS, Leta S. Chemical precipitation method for chromium removal and its recovery from tannery wastewater in Ethiopia. Chem Int. 2017;3:291–305.
[15] Jafarinejad S. Activated sludge combined with powdered activated carbon (PACT process) for the petroleum industry wastewater treatment: a review. Chem Int. 2017;3:368.
[16] Ismail M, Wu Z, Zhang L, Ma J, Jia Y, Hu Y, et al. High-efficient synergy of piezocatalysis and photocatalysis in bismuth oxychloride nanomaterial for dye decomposition. Chemosphere. 2019;228:212–8.
[17] You H, Wu Z, Jia Y, Xu X, Xia Y, Han Z, et al. High-efficiency and mechano-/photo-bi-catalysis of piezoelectric-ZnO@ photoelectric-TiO_2 core-shell nanofibers for dye decomposition. Chemosphere. 2017;183:528–35.
[18] Xu X, Wu Z, Xiao L, Jia Y, Ma J, Wang F, et al. Strong piezoelectro-chemical effect of piezoelectric $BaTiO_3$ nanofibers for vibration-catalysis. J Alloy Compd. 2018;762:915–21.
[19] El Nemr A, Hassaan MA, Madkour FF. Advanced oxidation process (AOP) for detoxification of acid red 17 dye solution and degradation mechanism. Env Process. 2018;5:95–113.
[20] Tu S, Guo Y, Zhang Y, Hu C, Zhang T, Ma T, et al. Piezocatalysis and piezo-photocatalysis: catalysts classification and modification strategy, reaction mechanism, and practical application. Adv Funct Mater. 2020;48:2005158.
[21] Saleh TA, Gupta VK. Photo-catalyzed degradation of hazardous dye methyl orange by use of a composite catalyst consisting of multi-walled carbon nanotubes and titanium dioxide. J Colloid Interf Sci. 2012;371:101–6.
[22] Hernández-Alonso MD, Fresno F, Suárez S, Coronado JM. Development of alternative photocatalysts to TiO_2: challenges and opportunities. Energ Env Sci. 2009;2:1231–57.
[23] Ray PZ, Shipley HJ. Inorganic nano-adsorbents for the removal of heavy metals and arsenic: a review. RSC Adv. 2015;5:29885–907.
[24] Kong D, Zheng Y, Kobielusz M, Wang Y, Bai Z, Macyk W, et al. Recent advances in visible light-driven water oxidation and reduction in suspension systems. Mater Today. 2018;21:897–924.
[25] Shu H-Y, Chang M-C, Tseng T-H. Solar and visible light illumination on immobilized nano zinc oxide for the degradation and mineralization of orange G in wastewater. Catalysts. 2017;7:164.
[26] Nair MG, Nirmala M, Rekha K, Anukaliani A. Structural, optical, photo catalytic and antibacterial activity of ZnO and Co doped ZnO nanoparticles. Mater Lett. 2011;65:1797–800.
[27] Yi S, Cui J, Li S, Zhang L, Wang D, Lin Y. Enhanced visible-light photocatalytic activity of Fe/ZnO for rhodamine B degradation and its photogenerated charge transfer properties. Appl Surf Sci. 2014;319:230–6.
[28] Low J, Yu J, Jaroniec M, Wageh S, Al-Ghamdi AA. Heterojunction photocatalysts. Adv Mater. 2017;29:1601694.
[29] Shameli K, Ahmad MB, Jazayeri SD, Shabanzadeh P, Sangpour P, Jahangirian H, et al. Investigation of antibacterial properties silver nanoparticles prepared via green method. Chem Cent J. 2012;6:1–10.
[30] Khalil MM, Ismail EH, El-Baghdady KZ, Mohamed D. Green synthesis of silver nanoparticles using olive leaf extract and its antibacterial activity. Arab J Chem. 2014;7:1131–9.
[31] Gupta M, Tomar RS, Kaushik S, Mishra RK, Sharma D. Effective antimicrobial activity of green ZnO nano particles of Catharanthus roseus. Front Microbiol. 2018;2030.
[32] Md Salim R, Asik J, Sarjadi MS. Chemical functional groups of extractives, cellulose and lignin extracted from native Leucaena leucocephala bark. Wood Sci Technol. 2021;55(2):295–313.
[33] Suresh J, Pradheesh G, Alexramani V, Sundrarajan M, Hong SI. Green synthesis and characterization of zinc oxide nanoparticle using insulin plant (Costus pictus D. Don) and investigation of its antimicrobial as well as anticancer activities. Adv Nat Sci-Nanosci. 2018;9:015008.
[34] Rodrıguez-Paéz J, Caballero A, Villegas M, Moure C, Duran P, Fernandez J. Controlled precipitation methods: formation mechanism of ZnO nanoparticles. J Eur Ceram Soc. 2001;21:925–30.
[35] PP V. In vitro biocompatibility and antimicrobial activities of zinc oxide nanoparticles (ZnO NPs) prepared by chemical and green synthetic route – A comparative study. BionanoScience. 2020;10:112–21.
[36] Páez CA, Liquet DY, Calberg C, Lambert SD, Willems I, Germeau A, et al. Study of photocatalytic decomposition of hydrogen peroxide over ramsdellite-MnO2 by O2-pressure monitoring. Catal Commun. 2011;15:132–6.
[37] Ferin Fathima A, Jothi Mani R, Sakthipandi K, Manimala K, Hossain A. Enhanced antifungal activity of pure and iron-doped ZnO nanoparticles prepared in the absence of reducing agents. J Inorg Organomet P. 2020;30:2397–405.
[38] Bala N, Saha S, Chakraborty M, Maiti M, Das S, Basu R, et al. Green synthesis of zinc oxide nanoparticles using Hibiscus

subdariffa leaf extract: effect of temperature on synthesis, anti-bacterial activity and anti-diabetic activity. RSC Adv. 2015;5:4993–5003.
[39] Peletiri C, Matur B, Ihongbe J, Okoye M. The effect of Azadirachta indica (Neem Tree) on human plasmodiasis: the laboratory perspective. Res J Med Sci. 2012;2:13–7.
[40] Wang M, Jiang L, Kim EJ, Hahn SH. Electronic structure and optical properties of Zn (OH) 2: LDA + U calculations and intense yellow luminescence. RSC Adv. 2015;5:87496–87503.
[41] Shankar JS, Ashok Kumar S, Periyasamy BK, Nayak SK. Studies on optical characteristics of multicolor emitting MEH-PPV/ZnO hybrid nanocomposite. Polym-Plast Technol. 2019;58:148–57.
[42] Johnson EM, Ojwang JO, Szekely A, Wallace TL, Warnock DW. Comparison of *in vitro* antifungal activities of free and liposome-encapsulated nystatin with those of four amphotericin B formulations. Antimicrob Agents Ch. 1998;42:1412–6.
[43] Rai A, Singh A, Ahmad A, Sastry M. Role of halide ions and temperature on the morphology of biologically synthesized gold nanotriangles. Langmuir. 2006;22:736–41.
[44] Dong S, Xu K, Liu J, Cui H. Photocatalytic performance of ZnO: Fe array films under sunlight irradiation. Phys B. 2011;406:3609–12.
[45] Raja K, Ramesh P, Geetha D. Structural, FTIR and photoluminescence studies of Fe doped ZnO nanopowder by co-precipitation method. Spectrochim Acta Part A. 2014;131:183–8.
[46] Huang MH, Wu Y, Feick H, Tran N, Weber E, Yang P. Catalytic growth of zinc oxide nanowires by vapor transport. Adv Mater. 2001;13(2):113–6.
[47] Williams G, Kamat PV. Graphene-semiconductor nanocomposites: excited-state interactions between ZnO nanoparticles and graphene oxide. Langmuir. 2009;25(24):13869–73.
[48] Karthika K, Ravichandran K. Tuning the microstructural and magnetic properties of ZnO nanopowders through the simultaneous doping of Mn and Ni for biomedical applications. J Mate Sci Technol. 2015;31:1111–7.
[49] Azimirad R, Khayatian A, Safa S, Kashi MA. Enhancing photoresponsivity of ultra violet photodetectors based on Fe doped ZnO/ZnO shell/core nanorods. J Alloy Compd. 2014;615:227–33.
[50] Afifah N, Djaja NF, Saleh R. Materials science forum. Trans Tech Publ. 2015;19–24.
[51] Huang W, Tang X, Felner I, Koltypin Y, Gedanken A. Preparation and characterization of FexOy–TiO2 via sonochemical synthesis. Mater Res bull. 2002;37:1721–35.
[52] Xiao S, Zhao L, Lian J. Enhanced photocatalytic performance of supported Fe doped ZnO nanorod arrays prepared by wet chemical method. Catal Lett. 2014;144:347–54.
[53] Ba-Abbad MM, Kadhum AAH, Mohamad AB, Takriff MS, Sopian K. Visible light photocatalytic activity of Fe^{3+}-doped ZnO nanoparticle prepared via sol–gel technique. Chemosphere. 2013;91:1604–11.
[54] Sun T, Qiu J, Liang C. Controllable fabrication and photocatalytic activity of ZnO nanobelt arrays. J Physl Chem C. 2008;112:715–21.
[55] Jang ES, Won JH, Hwang SJ, Choy JH. Fine tuning of the face orientation of ZnO crystals to optimize their photocatalytic activity. Adv Mater. 2006;18:3309–12.
[56] Machado AEH, de Miranda JA, de Freitas RF, Duarte ETF, Ferreira LF, Albuquerque YD, et al. Destruction of the organic matter present in effluent from a cellulose and paper industry using photocatalysis. J Photoch Photobio A. 2003;155:231–41.
[57] Rauf M, Meetani M, Hisaindee S. An overview on the photocatalytic degradation of azo dyes in the presence of TiO2 doped with selective transition metals. Desalination. 2011;276:13–27.
[58] Matos J, Laine J, Herrmann J-M. Effect of the type of activated carbons on the photocatalytic degradation of aqueous organic pollutants by UV-irradiated titania. J Catal. 2001;200:10–20.
[59] Eskizeybek V, Sarı F, Gülce H, Gülce A, Avcı A. Preparation of the new polyaniline/ZnO nanocomposite and its photocatalytic activity for degradation of methylene blue and malachite green dyes under UV and natural sun lights irradiations. Appl Catal B-Environ. 2012;119:197–206.
[60] Kitture R, Koppikar SJ, Kaul-Ghanekar R, Kale S. Catalyst efficiency, photostability and reusability study of ZnO nanoparticles in visible light for dye degradation. J Phys Chem Solids. 2011;72:60–6.